Nano Research

Open Access

Research Article

Biomass-derived 2D Pb^0/Pb^{2+} dual-center-site catalysts for efficient 5-hydroxymethylfurfural electroreduction

Haoran Wu[1], Haishan Xu[2], Zhenbing Xie[3] ✉, Runlu Yang[1], Xin Wang[1], Xinwei Chen[2], Liang Wu[2], Chongyin Zhang[4] ✉, Weixia Zhu[1] ✉, and Yiyong Mai[2] ✉

[1] *School of Chemical Engineering, Zhengzhou University, Zhengzhou 450001, China*
[2] *School of Chemistry and Chemical Engineering, Frontiers Science Center for Transformative Molecules, Shanghai Key Laboratory of Electrical Insulation and Thermal Ageing, Shanghai Jiao Tong University, Shanghai 200240, China*
[3] *Department of Chemistry, Tangshan Normal University, Tangshan 063000, China*
[4] *Shanghai Aerospace Equipments Manufacturer Co., Ltd., Shanghai 200245, China*

Cite this article: *Nano Research*, **2025**, *18*, 94907089. https://doi.org/10.26599/NR.2025.94907089

ABSTRACT: Using natural resources to construct electrocatalysts for biomass conversion and elucidating their catalytic mechanisms are of great significance, but have remained challenging. Here, a series of two-dimensional (2D) biomass-based Pb/PbO@C catalysts with Pb/PbO nanoparticles anchored on carbon nanosheets were synthesized using natural-derived humate as the precursor. By adjusting the carbonization temperature, an electron-deficient Pb^0/Pb^{2+} dual-center-site catalyst can be achieved. The optimized Pb/PbO@C catalyst showed an excellent performance for the electrochemical hydrogenation of 5-hydroxymethylfurfural (HMF) to high value-added 2,5-bis(hydroxymethyl)furan (BHMF), with high Faradaic efficiency (FE: 91.9%) and selectivity (Sel: 89.7%), achieving comparable performance to those of the reported noble metal-based electrocatalysts. Mechanism study revealed that the electron-deficient Pb^0/Pb^{2+} dual-center-site provided abundant Lewis acidic sites and promoted the dissociation of water to the active hydrogen (H*) species, thus enhancing the adsorption of HMF on Pb^{2+} sites and the coverage of H* species on Pb^0 sites. The high coverage of H* species and the synergistic effect of dual-center sites substantially promoted the binding of H* and HMF to form H-HMF* and inhibited the recombination of H* species, thereby accelerating the reaction kinetics of HMF reduction.

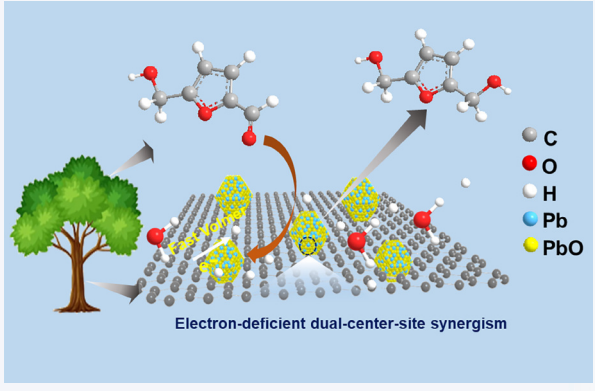

KEYWORDS: biomass conversion, biomass-derived carbon materials, electrocatalysis, hydrogenation, 5-hydroxymethylfurfural

1 Introduction

With the ever-increasing depletion of fossil resources, the utilization of renewable biomass to produce high value-added chemicals has attracted considerable interest [1–4]. In this regard, the hydrogenation of 5-hydroxymethylfurfural (HMF) derived from lignocellulose to 2,5-bis(hydroxymethyl)furan (BHMF) is one of the most important reactions in the field of biomass valorization [5–7]. BHMF has been recognized as an indispensable feedstock for sustainable chemicals production, such as polymers, biobased fuel, etc [8–10]. Among the various upgrading methods, the electrocatalytic hydrogenation strategy has sparked increasing interest due to its mild reaction conditions and cheap hydrogen source (e.g., ambient conditions and H_2O as hydrogen source) [11]. In this regard, many electrocatalysts have been reported for the electrocatalytic reduction of HMF including transition metal, metal oxides and noble metal-based electrocatalysts [12–14]. Despite these impressive progresses, many limitations still need to be overcome, such as the complexity of the electrocatalyst preparation, the high-cost noble metals or ligands, unsatisfied Faradaic efficiency (FE) and/or selectivity (Sel), etc. In addition, the insight into mechanism of electrocatalytic HMF reduction has remained a great

Received: July 28, 2024; **Revised:** October 3, 2024
Accepted: October 21, 2024

✉Address correspondence to Zhenbing Xie, xzbing@tstc.edu.cn; Chongyin Zhang, chongyin1022@163.com; Weixia Zhu, zhuweixia@zzu.edu.cn; Yiyong Mai, mai@sjtu.edu.cn

challenge without a clear understanding of the catalytic active sites. Therefore, it is highly desirable to design efficient electrocatalysts through facile processes and understand their catalytic mechanisms for the electrocatalytic hydrogenation of HMF to BHMF, especially catalysts from renewable materials [6].

In recent years, the construction of functional electrocatalysts using natural chemicals as precursors for biomass conversion has attracted great attention [15–17]. In this regard, humic acid as a renewable organic acid, has been widely used in the fields of agriculture and environment [18–20]. Owning to the existence of phenol-, carboxyl- and enol groups (Fig. S1 in the Electronic Supplementary Material (ESM)), humic acid exhibits some fascinating advantages including easy chelation with metal ions, antioxidant and regenerable electron acceptors [20–22]. Taking advantage of the coordination characteristic between humic acid and metal ions, *in-situ* construction of humic acid-derived carbon supported nano-metal catalysts helps to suppress the aggregation of large metal nanoparticles, stabilize metal catalytic active sites and regulate electronic structure of loaded metals, possessing great potential to serve as promising electrocatalysts for biomass valorization. However, to our knowledge, no concern about this concept has been reported thus far.

Here, we reported the construction of two-dimensional (2D) biomass-based Pb/PbO@C catalysts using lead acetate and sodium humate as the precursors, respectively. The optimized Pb/PbO@C-800 (prepared at 800 °C) displayed a highly integrated two-dimensional nanostructure (~ 13 nm thickness), consisting of Pb/PbO nanoparticles (mean size of ~ 3.5 nm) anchored uniformly on carbon nanosheets. It has been shown that the electronic structure of Pb species can be tuned by the carbonization temperature to achieve an electron-deficient property. When employed as an electrocatalyst, it showed an excellent catalytic performance for the electrochemical hydrogenation of HMF to BHMF with high FE (91.9%) and Sel (89.7%), which was close to the performance of the reported noble metal-based electrocatalysts (Table S1 in the ESM). Mechanism study revealed that the superior performance of Pb/PbO@C-800 stemmed from the abundant Lewis acidic sites, the strong electronic interaction between Pb^0/Pb^{2+} and carbon support and the synergistic effect of Pb^0 and Pb^{2+} sites, which enhanced the adsorption of HMF on Pb^{2+} sites and the dissociation of water to increase the coverage of active hydrogen (H*) species on Pb^0 sites , thus reducing the reaction energy barrier of HMF and H*, inhibiting the recombination of H* and boosting the reaction kinetics of HMF reduction. This work provides new clues for understanding the HMF reduction mechanism through regulating the strong electronic interaction of metal and support to increase the H* coverage on active sites and introducing dual-center sites synergism to reduce the reaction energy barrier of H* and HMF, thus speeding up their reaction kinetics.

2 Experimental section

2.1 Materials

Sodium humate was purchased from Acros Co., Ltd. Humic acid was obtained from Alfa Aesar China Co., Ltd. 1-Butyl-3-methylimidazolium tetrafluoroborate ([Bmim]BF_4) was supplied by the Centre for Green Chemistry and Catalysis, Lanzhou Institute of Chemical Physics, Chinese Academy of Sciences. Lead acetate trihydrate (99%) was obtained from Sinopharm Chemical Reagent Co., Ltd. Lead was supplied by Beijing Innochem Science & Technology Co., Ltd. Lead monoxide was obtained from Adams Co., Ltd. Nafion N-117 membranes (0.90 meg·g^{-1} exchange capacity), Nafion D-521 dispersion (5 wt.% in water and 1-propanol) and Toray carbon paper were supplied by J&K Scientific Co., Ltd.

2.2 Synthesis of biomass-based Pb/PbO@C catalysts

The biomass-based Pb/PbO@C catalysts were prepared through a coprecipitation-carbonization strategy. First, sodium humate (0.7 g) was dissolved into pure water (30 mL) to form the solution A. Then the solution A was filtered to remove insoluble substances. Afterwards, a solution B was prepared by adding lead acetate (3.0 g) into pure water (50 mL). Subsequently, the B solution was added into the A solution to form black precipitation (denoted as Pb-HA). The Pb-HA was separated and moved to a vacuum oven. Second, the as-prepared Pb-HA was pyrolyzed at different temperatures (e.g., 600, 700, 800 and 900 °C) under N_2 atmosphere for 2 h to generate the Pb/PbO@C catalysts (denoted as Pb/PbO@C-600, Pb/PbO@C-700, Pb/PbO@C-800 and Pb/PbO@C-900, respectively).

3 Results and discussion

3.1 Synthesis and characterization of biomass-based Pb/PbO@C catalysts

The Pb/PbO@C catalysts were prepared by a facile coprecipitation-carbonization strategy using natural-derived sodium humate as the carbon source and lead acetate as the metal precursor, respectively (Fig. 1(a)). Typically, an organic–inorganic hybrid (denoted as Pb-HA) was first synthesized via a coprecipitation method between natural-derived sodium humate and lead acetate. During the synthetic process, sodium humate easily dissociates into sodium ion and humate group in water. Then the humate group chelates with lead ions via the coordination interaction [23–25], leading to the formation of Pb-HA. Subsequently, Pb-HA was heated to a certain temperature (600, 700, 800 and 900 °C, respectively) under N_2 atmosphere and then cooled naturally to room temperature. The resultant materials were labeled as Pb/PbO@C catalysts (denoted as Pb/PbO@C-600, Pb/PbO@C-700, Pb/PbO@C-800 and Pb/PbO@C-900, respectively).

The synthesized Pb/PbO@C catalysts were initially characterized by the power X-ray diffraction (XRD). As shown in Fig. S2 in the ESM, the characteristic diffraction peaks of metallic Pb (PDF:04-0686) and PbO (PDF:38-1477) can be clearly observed, confirming the co-existence of Pb^0 and PbO in the prepared catalysts. Transmission electron microscopy (TEM) shows a two-dimensional nanosheet structure and small nanoparticles of Pb/PbO are uniformly anchored on the surface of carbon nanosheets (Fig. 1(b) and Figs. S3–S6 in the ESM). X-ray photoelectron spectroscopy (XPS) was employed to assess the surface elemental valence state and chemical composition of Pb/PbO@C catalysts. As shown in Figs. S7–S10 in the ESM, the signals of C 1s, O 1s and Pb 4f are discerned in Pb/PbO@C catalysts. In addition, the high-resolution XPS spectra of Pb 4f in Pb/PbO@C catalysts show two broad peaks, which can be assigned to Pb $4f_{7/2}$ and Pb $4f_{5/2}$ (Figs. S11–S14 in the ESM) [26–28]. Each peak of Pb 4f can be deconvoluted into two parts of Pb^0 and Pb^{2+}.

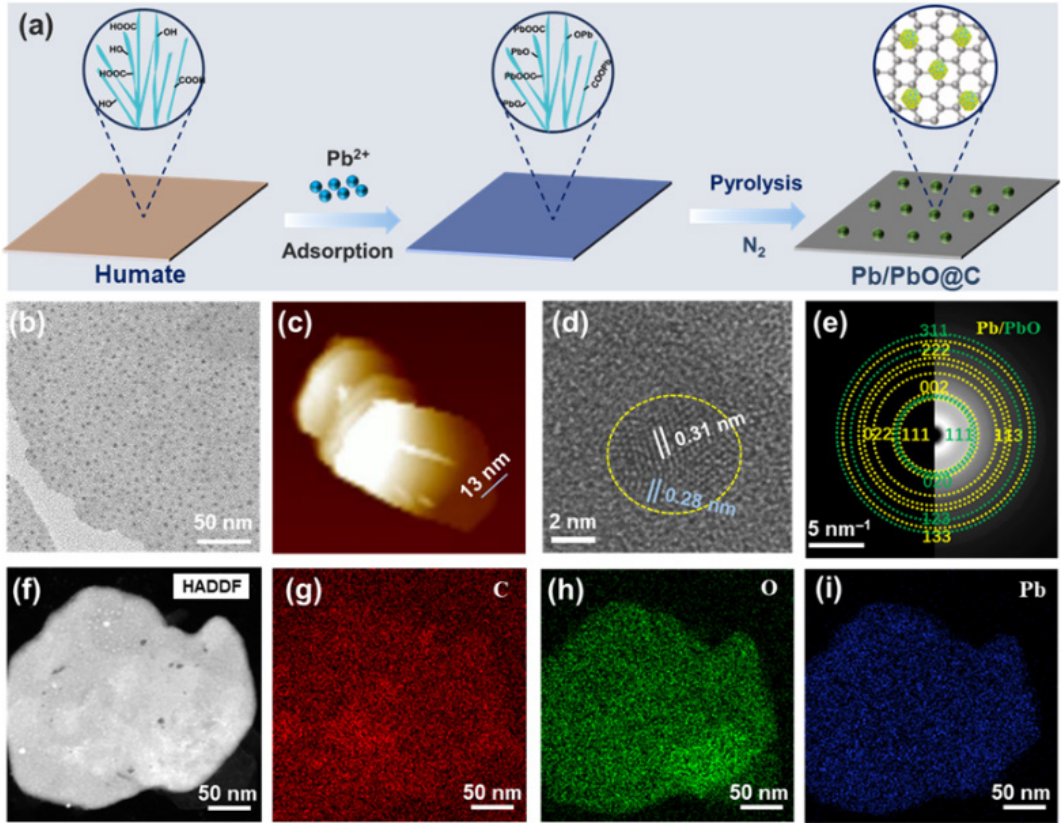

Figure 1 (a) Schematic illustration of the synthesis of biomass-based Pb/PbO@C catalysts. Structure characterization of Pb/PbO@C-800: (b) TEM image, (c) AFM image, (d) HRTEM image, (e) SAED pattern, and (f)–(i) element mapping images.

The atomic ratio of Pb^0/Pb^{2+} in Pb/PbO@C increases from 0.26 to 0.86 with the increasing pyrolysis temperature (Fig. S15 in the ESM), suggesting that Pb^{2+} in Pb/PbO@C catalysts can be further transformed into Pb^0 with the increase of pyrolysis temperatures. As an example, the structure of Pb/PbO@C-800 was further studied by atomic force microscopy (AFM). As shown in Fig. 1(c), Pb/PbO@C-800 displays a clear two-dimensional nanosheets structure. AFM height profile shows that the thickness of nanosheets is approximately 13 nm (Fig. 1(c) and Fig. S16 in the ESM). The mean size of Pb/PbO nanoparticles is approximately 3.5 nm (Fig. S17 in the ESM). The small size and uniform distribution of Pb/PbO nanoparticles on the carbon nanosheets may be attributed to the good coordination interaction between humate group and lead ions [23, 29, 30], which contributes to inhibiting the larger aggregation of Pb/PbO nanoparticles. The high-resolution TEM (HRTEM) image (Fig. 1(d)) further reveals the lattice fringes with interplanar distance of 0.31 and 0.28 nm, corresponding to the (111) crystal plane of PbO and the (111) plane of Pb, respectively, which is consistent with the XRD results (Fig. S2 in the ESM). The selected area electron diffraction (SAED) patterns in Fig. 1(e) are assigned to both the metallic Pb ($Fm\bar{3}m$) and PbO ($Pcam$). The energy dispersive spectrometer line scanning of single nanoparticle in Pb/PbO@C-800 suggests that the single nanoparticle consists of Pb and PbO (Fig. S18 in the ESM). These results are consistent with HRTEM characterization (Fig. 1(d)). The elemental mapping images of Pb/PbO@C-800 show a uniform distribution of C, O and Pb elements in the entire architecture (Figs. 1(f)–1(i)). The above results indicate that Pb/PbO@C catalysts have been successfully synthesized.

3.2 Performance evaluation of Pb/PbO@C for the HMF electroreduction

The HMF reduction ability of Pb/PbO@C catalysts was first examined by performing cyclic voltammetry (CV) measurements, which was performed on a standard three-electrode system in the range from 0 to −2.4 V vs. Ag/Ag^+ with a scan rate of 20 $mV{\cdot}s^{-1}$. As shown in Fig. 2(a) and Figs. S19–S21 in the ESM, there is a significant increase of current density within the range of −1.9 to −2.4 V vs. Ag/Ag^+ after adding HMF to the cathode electrolyte, indicating the occurrence of HMF reduction. The electrocatalytic experiments showed that the main product was BHMF and a trace of by-products were detected, including 5-methyl-2-furyl-methanol (MFM) and 2-methylfurfural (MF) (Fig. S22 in the ESM).

To further examine the electrocatalytic performance of Pb/PbO@C catalysts, the influence of different potentials on the electrocatalytic hydrogenation of HMF was firstly investigated. As shown in Fig. 2(b), both the Faraday efficiency of BHMF and the conversion of HMF over Pb/PbO@C-800 electrocatalyst firstly increase then gradually decrease with the increase of applied potential, while the selectivity of BHMF displays a gradually decreasing trend. At −2.2 V, Pb/PbO@C-800 exhibits the optimal performance with high FE (91.9%) and Sel (89.7%) of BHMF. Similar phenomenon was also observed when employed Pb/PbO@C-600, Pb/PbO@C-700 and Pb/PbO@C-900 as electrocatalysts (Figs. S23–S25 in the ESM). The pyrolysis temperature of the catalysts often has a significant effect on the FE and Sel of BHMF. Figure 2(c) compares the electrochemical performance of different Pb/PbO@C catalysts. It can be observed that Pb/PbO@C-800 exhibits the best FE (91.9%) and Sel (89.7%) of

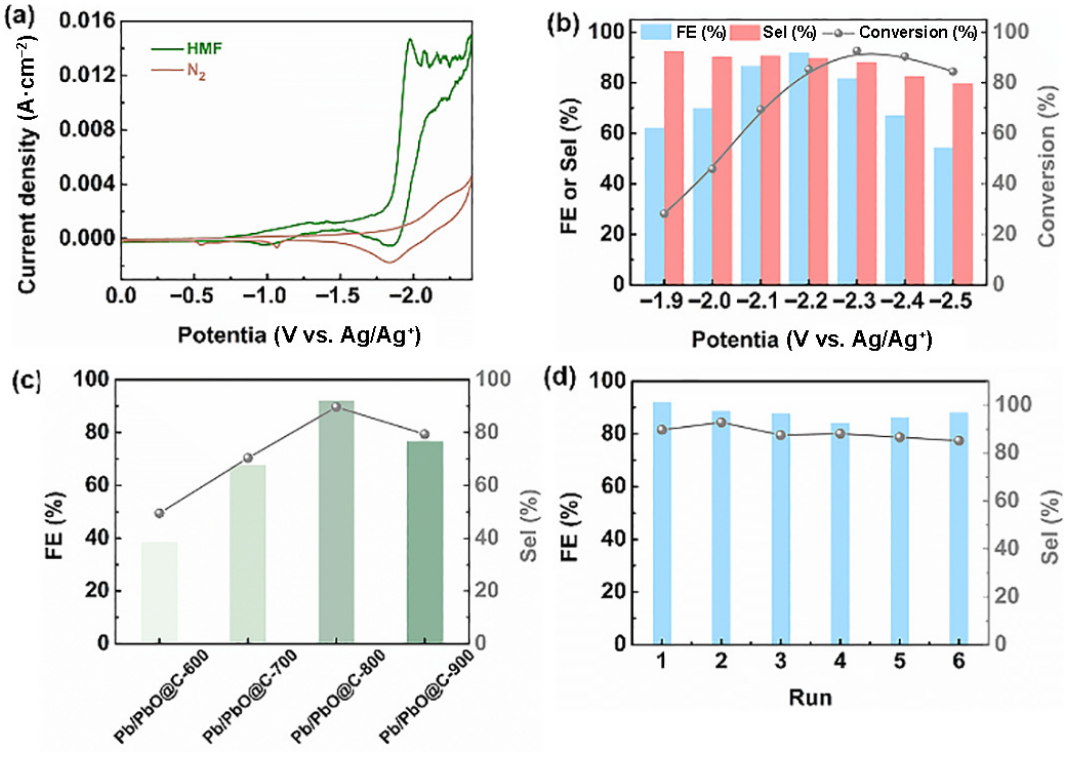

Figure 2 Performance study of Pb/PbO@C for the electrocatalytic hydrogenation of HMF. (a) CV of Pb/PbO@C-800. (b) Different potentials over Pb/PbO@C-800. (c) Different pyrolysis temperature over Pb/PbO@C at −2.2 V vs. Ag/Ag^+. (d) Cycling performance of Pb/PbO@C-800 at −2.2 V vs. Ag/Ag^+.

BHMF among these Pb/PbO@C catalysts. The decrease in the FE and Sel over Pb/PbO@-900 may be resulted from the decreasing occupancy of PbO (Fig. S15 in the ESM). In addition, the relative intensity ratio of the D band to the G band (I_D/I_G) decreases with the increase of carbonization temperature (Fig. S26 in the ESM), indicating that the suitable graphitization degree is helpful for the HMF reduction. Meanwhile, Pb/PbO@C-800 shows an excellent stability and recyclability without obvious decrease in the FE and Sel of BHMF using six times (Fig. 2(d)). The yield rate of BHMF could reach 0.117 mmol/h/cm^2. XPS characterization shows that the atomic ratio of Pb^0/Pb^{2+} in the used Pb/PbO@C-800 (0.72) was very close to that of fresh Pb/PbO@C-800 (0.67) (Fig. S27(a) in the ESM). Furthermore, the morphology of Pb/PbO@C-800 is well retained (Fig. S27(b) in the ESM). These results verify the excellent stability of Pb/PbO@C-800. In addition, we also try to explore the performance of Pb/PbO@C-800 at high HMF concentrations. As shown in Fig. S28 in the ESM, the Faradaic efficiency and selectivity of BHMF gradually decreased with the increase of HMF concentration, indicating that an excessive HMF concentration is not beneficial for the reduction of HMF to BHMF. Similar result was also observed in some reported studies [31].

3.3 Mechanism study

To identify the active sites of catalysts contributes to designing functional catalysts for special reactions [31, 32]. In this work, we selected PbO, Pb, humic acid-based carbon (denoted as C) and their mechanical mixtures (denoted as Pb-PbO-C) as control samples. The humic acid-based carbon was synthesized by pyrolysis of humic acid at 800 °C (Fig. S29 in the ESM). As shown in Fig. 3(a), both PbO and Pb exhibit lower FE and Sel for the electrochemical reduction of HMF to BHMF. In addition, a very poor activity, almost inert for the BHMF production, is observed over the C, indicating that Pb/PbO in Pb/PbO@C catalysts is identified as the key active species for the HMF reduction.

In addition, the mechanical mixture of Pb-PbO-C displays an obviously lower performance (FE: 38.9%; Sel: 55.3%) than Pb/PbO@C-800, indicating that the interaction between Pb species and support in Pb/PbO@C-800 plays a crucial role in the HMF reduction. Compared to the Pb/PbO@C-600, the high-resolution XPS Pb 4f spectra show an obvious shift to high binding energy (Fig. 3(b)), indicating the electron-deficient property of Pb^0/Pb^{2+} in Pb/PbO@C catalysts. In addition, the high-resolution XPS Pb 4f spectrum in Pb/PbO@C-800 presents an obvious shift to lower binding energy in comparison to Pb/PbO@C-700, indicating that there are different degrees of electronic interactions between Pb species and support [33, 34]. The main reason is attributed to the effect of pyrolysis temperature that changes the molar ratio of Pb^0 to Pb^{2+} (Fig. S15 in the ESM) and the degree of graphitization of carrier (Fig. S26 in the ESM), which together affect the degree of electronic interaction between the Pb species and carbon carrier. Therefore, it is not difficult to understand that the binding energy of Pb 4f in Pb/PbO@C-800 is reduced relative to Pb/PbO@C-700. The ultraviolet photoelectron spectroscopy (UPS) was employed to explore the work function of Pb/PbO@C catalysts. As shown in Figs. S30 and S31 in the ESM, the work function of Pb/PbO@C catalysts presents a similar trend with the XPS results. Based on the UPS, XPS and literature [35–37], it can be proved that there is electron transfer across the interface of Pb/PbO and the carbon support, which further indicates the existence of electronic interaction of the Pb species and the carbon support.

The selectivity of electrochemical reduction of HMF to BHMF is related to the adsorption of HMF carbonyl group on electrocatalyst and the electron-rich oxygen in HMF carbonyl group tends to adsorb on the Lewis acidic sites of catalysts [5, 6, 38]. Therefore, the

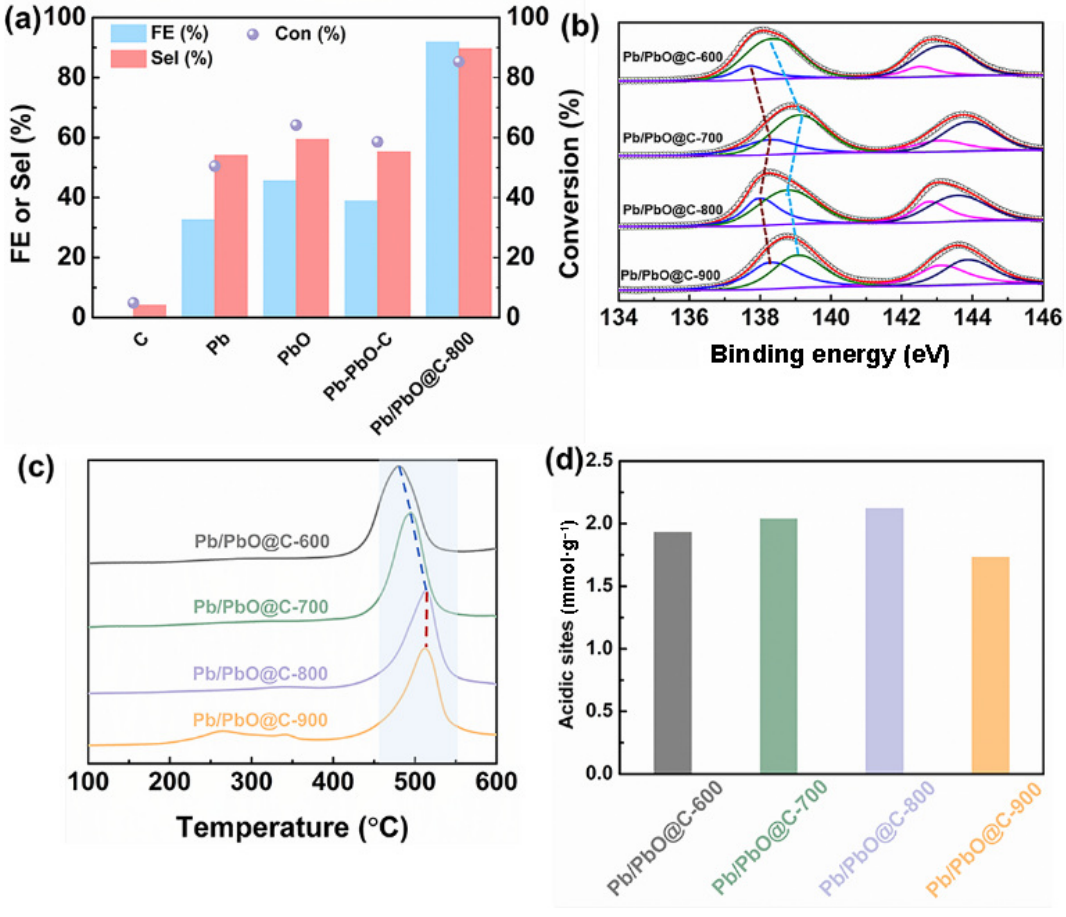

Figure 3 (a) Control samples for the electrochemical reduction of HMF (the accumulated charge was 20.4 C). (b) High-resolution XPS Pb 4f spectra of Pb/PbO@C catalysts. (c) NH_3-TPD of Pb/PbO@C catalysts. (d) The amounts of acidic sites of Pb/PbO@C catalysts.

ammonia temperature-programmed desorption (NH_3-TPD) was used to study the Lewis acidic adsorption sites of Pb/PbO@C catalysts. As shown in Fig. 3(c), with the increase of pyrolysis temperature (600–800 °C) of Pb/PbO@C catalysts, the desorption temperature of NH_3 from Pb/PbO@C gradually increases from 480 to 515 °C. However, when the pyrolysis temperature of Pb/PbO@C reaches 900 °C, the desorption temperature of NH_3 from Pb/PbO@C decreases to 510 °C and new desorption peaks appear in the range of 250–350 °C, indicating a decreased Lewis acidic property. In addition, Fig. 3(d) shows that Pb/PbO@C-800 possesses more Lewis acidic sites, which contributes to enhancing the interface adsorption between the electron-rich oxygen in carbonyl group with catalytic surface. Based on the above analysis, it can be concluded that the strong Lewis acidity and high adsorption sites of Pb/PbO@C-800 contribute to promoting the adsorption of HMF, thereby favoring a high selectivity towards BHMF in the HMF reduction.

The electrochemically active surface area of Pb/PbO@C was assessed by calculating the double-layer capacitance (C_{dl}). The C_{dl} value of Pb/PbO@C catalysts (Fig. 4(a) and Figs. S32–S35 in the ESM) follows the order of Pb/PbO@C-800 (1.36 mF·cm^{-2}) > Pb/PbO@C-700 (1.31 mF·cm^{-2}) > Pb/PbO@C-600 (1.20 mF·cm^{-2}) > Pb/PbO@C-900 (0.98 mF·cm^{-2}), indicating that Pb/PbO@C-800 can expose more active sites for the electrochemical reduction of HMF. The lower C_{dl} value of Pb/PbO@C-900 is attributed to the destruction of two-dimensional nanosheet structure and the generation of large nanoparticles (Fig. S6 in the ESM). Based on the above analysis, it can be concluded that the appropriate pyrolysis temperature of Pb/PbO@C catalysts is helpful for increasing the active surface area and exposing more catalytically active sites.

To study the catalytic reaction kinetics of Pb/PbO@C catalysts for the HMF reduction, Tafel plots were employed. From Fig. 4(b), Tafel slope of Pb/PbO@C-800 (42.13 mV·dec^{-1}) is the lowest among those of all the Pb/PbO@C catalysts (153.97 mV·dec^{-1} for Pb/PbO@C-600, 152.94 mV·dec^{-1} for Pb/PbO@C-700 and 175.78 mV·dec^{-1} for Pb/PbO@C-900, respectively), suggesting a fast reaction kinetic for the electrocatalytic reduction of HMF. CV curves of Pb/PbO@C-800 in the presence of N_2 (Fig. 4(c)) show a significant peak at −1.84 V, which is assigned to the desorption of H* species [39]. It can be seen that Pb/PbO@C-800 has a highest desorption peak of H* species among Pb/PbO@C catalysts (Fig. 4(c)), indicating that Pb/PbO@C-800 can enhance the process of water dissociation to H* species [31], resulting in a high coverage of H* species on Pb/PbO@C-800 surface. Figure 4(d) shows the CV curves of Pb/PbO@C-800 catalysts at different HMF concentrations. It can be found that the desorption peak intensity of H* species gradually decreases while the reduction peak intensity of HMF gradually increases with the increase of HMF concentrations, indicating that the reaction kinetics of H* and HMF are fast, allowing that the generated H* on the surface of Pb/PbO@C-800 can be fast consumed, thereby reducing the recombination of H* to form H_2 [31, 40].

The electrochemical reduction of HMF and hydrogen evolution reaction (HER) have the common Volmer step, namely, the

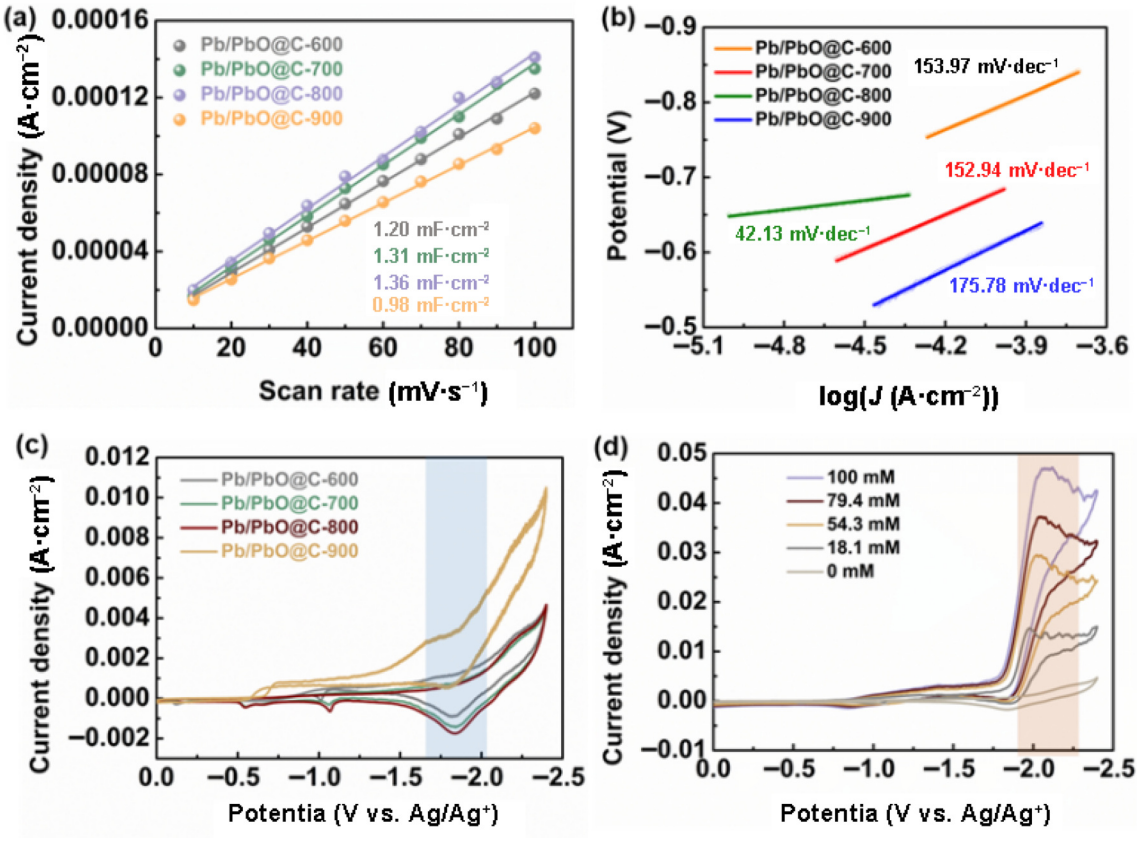

Figure 4 (a) The estimation of C_{dl} by plotting the current against scan rate. (b) Tafel plots of Pb/PbO@C in the presence of HMF. (c) CV of Pb/PbO@C in the presence of N_2. (d) CV of Pb/PbO@C-800 at different HMF concentrations.

dissociation of water to produce H* species. Figure 5(a) shows the Tafel plots of Pb/PbO@C-800 for the electrochemical reduction of HMF and HER, respectively. The Tafel slope of HER (122.75 mV·dec^{-1}) over Pb/PbO@C-800 catalyst was close to the standard value of 120 mV·dec^{-1} [41], indicating that the Volmer step is the rate-determining step. After adding HMF, Pb/PbO@C-800 exhibited a significantly decreased Tafel slope in the presence of HMF (42.13 mV·dec^{-1}) compared with HER (122.75 mV·dec^{-1}), indicating that the hydrogenation reaction of H* and HMF dominated the reaction process of HMF reduction and the electrochemical reduction of HMF process was more favorable than the HER process [42–44].

To probe the interfacial information of electrocatalyst/electrolyte, the charge-transfer resistance of Pb/PbO@C for the HMF reduction was investigated by electrochemical impedance spectroscopy (EIS). The EIS of Pb/PbO@C electrocatalysts at the open circuit potential was studied. As shown in Fig. 5(b), Pb/PbO@C-800 exhibits a faster charge transfer rate due to the small arc degree, which is beneficial for promoting the reduction of HMF. The reason may be attributed to the appropriate electronic interaction between Pb species and carbon support of Pb/PbO@C-800 (as evidenced in Fig. 3(b)), boosting the interfacial charge transfer on electrocatalyst/electrolyte. We also investigated the *in-situ* Bode plots of Pb/PbO@C-800 with or without HMF to understand the process of HMF reduction. As illustrated in Fig. 5(c), the phase angle intensity of HMF reduction is much lower than that of hydrogen evolution reaction, indicating that Pb/PbO@C-800 prefers to catalyze the electrochemical reduction of HMF in comparison to hydrogen evolution reaction due to the lower interfacial reaction charge transfer resistance of H* species and HMF (Fig. S36 in the ESM), in accordance with the Tafel results (Fig. 5(a)).

The Bode phase plots of Pb/PbO@C-800 for the electrochemical reduction of HMF at different potentials were also studied. As shown in Fig. 5(d), there is a significant phase angle peak in the medium frequency region. According to relative literatures, medium frequency region can be ascribed to the reaction charge transfer on the electrocatalyst/electrolyte interface [45, 46]. The phase angle peak decreases with the increase of applied potential at the range from −0.4 to −1.9 V, which mainly corresponds to the fast formation of H* species from the dissociation of water and a small portion of HMF reduction. With the further increase of applied potential (−1.9 to −2.1 V), the phase angle peak increases, which may be attributed to the increasing amount of H* species occupation on active sites of electrocatalyst that decreases the accessible sites for H* species production [46, 47]. At −2.1 to −2.5 V, the peak intensity of phase angle decreases, suggesting that the high potential can accelerate the depletion of the H* species. Based on the investigation of applied potential (Fig. 2(b)), −2.2 V is the optimal potential for the electrochemical reduction of HMF to BHMF. With a further increase in the applied potential (−2.2 to −2.5 V), the Faradaic efficiency and selectivity of BHMF decrease, indicating the occurrence of side reactions, such as HER and generation of 5-methyl-2-furyl-methanol and 2-methylfurfural. Therefore, it can be concluded that the decrease of phase peak in the medium frequency at −2.1 to −2.5 V is the result of multiple effects including the reaction charge transfer of H* and HMF as well as the self-recombination of H* and H*.

To better understand the reduction process of HMF, a simplified

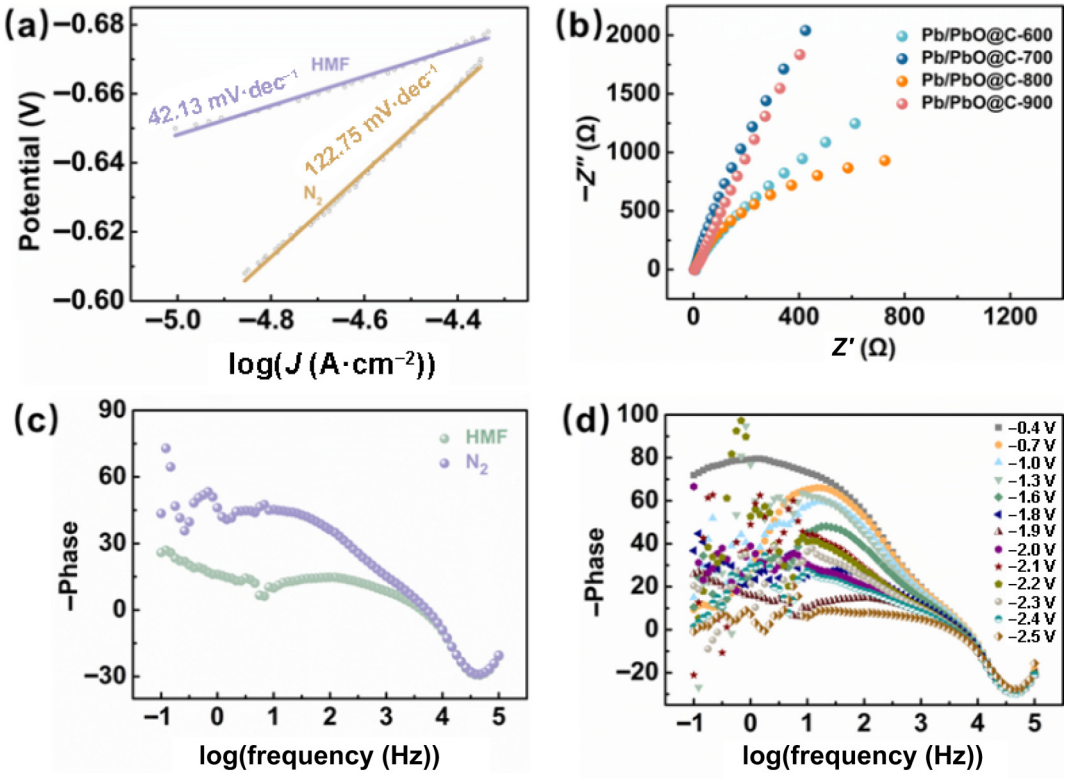

Figure 5 (a) Tafel plots of Pb/PbO@C-800 with or without HMF. (b) Nyquist plots of Pb/PbO@C at the open circuit potential. (c) Bode plots of Pb/PbO@C-800 at −1.9 V vs. Ag/Ag^+ with or without HMF. (d) *In-situ* Bode plots of Pb/PbO@C-800 at different potentials in the presence of HMF.

electrochemical reduction equivalent circuit was proposed to understand the catalytic behavior of Pb/PbO@C at high potentials (Fig. 6(a)). The equivalent circuit comprises two parts: (1) Volmer process of water dissociation to H* species and (2) interfacial reaction charge transfer process. The equivalent resistance of the Volmer process (R_1) and the interfacial reaction charge transfer process (R_2) with or without HMF were shown in Figs. 6(b) and 6(c) and Fig. S37 in the ESM. From Fig. 6(b), the value of R_1 in the presence of HMF is lower than that of N_2, indicating that the *in-situ* generated H* species are highly reactive with the adsorbed HMF [31], thus promoting the Volmer process, which is in agreement with Fig. 5(a). Meanwhile, R_2 decreased with the addition of HMF (Fig. 6(c)), implying that the recombination of the H* species themselves to produce H_2 is kinetically unfavored in the presence of HMF [31].

Based on the above-mentioned analysis, the reaction mechanism for the electrochemical reduction of HMF to BHMF over Pb/PbO@C is proposed. As shown in Fig. 6(d), the dissociation of water to form H* species is promoted over Pb/PbO@C, resulting in a high H* coverage on catalyst surface. After that, the H* species attack the HMF carbonyl group adsorbed on the Lewis acidic sites of Pb/PbO@C to form H-HMF*. Meanwhile, the faster reaction kinetic rate of H* species and HMF reduces the recombination of H* species to generation H_2. Subsequently, the H-HMF* further obtains a H* to form BHMF product. Further, the reaction mechanism of HMF reduction is rationalized by density functional theory (DFT) calculations at the electronic level using the computational models of Pb@C, PbO@C and Pb/PbO@C surfaces (Fig. 7). The proposed mechanism indicates that the electrochemical reduction of HMF to BHMF comprises four stages: (I) surface activation of H* species by catalyst; (II) adsorption of HMF on the catalyst surfaces; (III) hydrogenation of HMF by H* to form H-HMF*; (IV) further hydrogenation of H-HMF* to generate BHMF. The adsorption of H* species and HMF on catalysts is considered to be the crucial step for the surface synthesis of BHMF [42]. For the adsorption of H* species (Stage I), the adsorption energy of catalysts for H* (Figs. S38 and S39 in the ESM) follows the order of Pb/PbO@C (−5.700 eV) < Pb@C (−5.346 eV) < PbO@C (−3.302 eV), indicating that Pb^0 sites facilitate the adsorption of H* species and the synergistic effect of Pb^0 and Pb^{2+} sites in Pb/PbO@C can enhance the adsorption of H* species. Figures S40 and S41 in the ESM show that Pb/PbO@C (−0.910 eV) possesses a lower adsorption energy for HMF than those of PbO@C (−0.727 eV) and Pb@C (−0.705 eV), indicating that Pb^{2+} sites are beneficial for the adsorption of HMF and the combination of Pb and PbO promotes the adsorption of HMF. As illustrated in Stage II (Fig. 7), Pb/PbO@C displays the lower adsorption (−6.148 eV) for H* and HMF than those of Pb@C (−5.7 eV) and PbO@C (−4.957 eV), suggesting the crucial synergistic effect of the Pb^0 and Pb^{2+} sites in Pb/PbO@C. The above results are also evidenced by CV, XPS and NH_3-TPD investigation (Figs. 3(b)–3(d), 4(c) and 4(d)). The combination of H* and HMF to form H-HMF* (Stage III in Fig. 7) is the critical step in the preparation of BHMF [14]. The free energy changes of the electrocatalytic reduction over PbO@C and Pb/PbO@C are stepwise downwards and all steps of HMF reduction by the two catalysis surfaces are spontaneous exothermic reactions. However, the energy change of the binding of H* and HMF to form H-HMF* over Pb@C is an endothermic reaction, indicating that Pb^{2+} sites contribute to the combination of H* and HMF to form H-HMF*. Of note, the energy for the formation of H-HMF* over Pb/PbO@C is much lower (−6.340 eV) than those of Pb@C (−5.401 eV) and

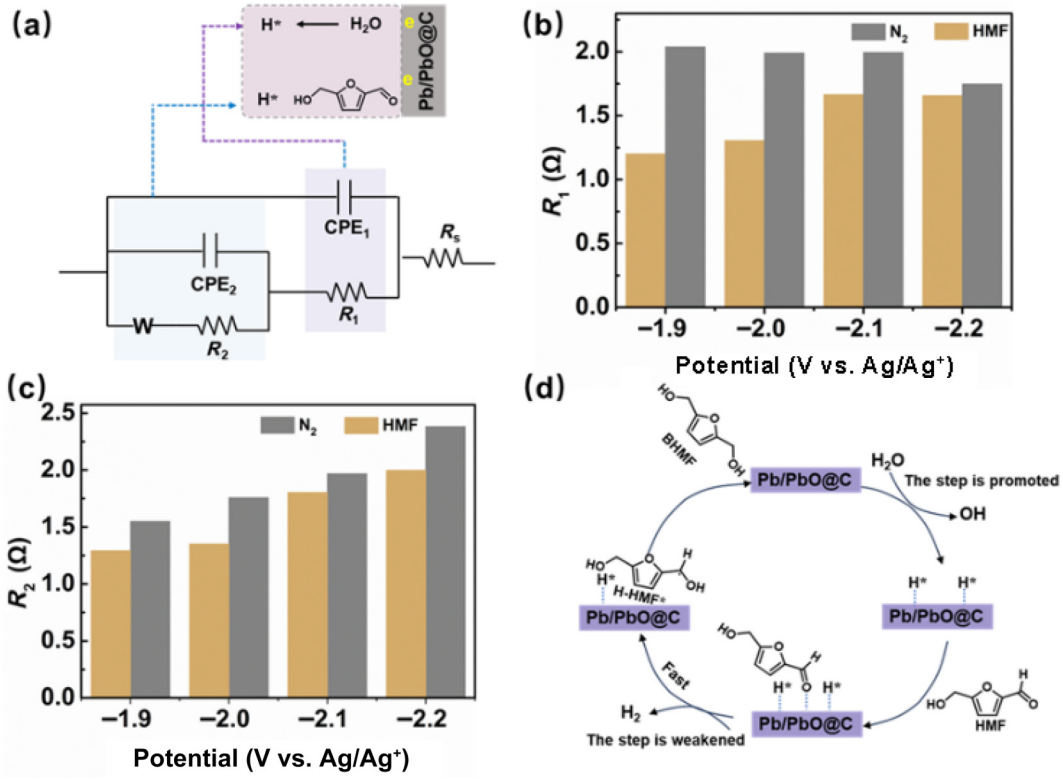

Figure 6 (a) Equivalent circuit for the HMF reduction over the Pb/PbO@C catalysts at high potentials (R_1, R_2, R_s, constant phase element (CPE) and W is the charge transfer resistance of Volmer step, interfacial reaction charge transfer resistance, solution resistance, constant phase element and Warburg impedance element, respectively). Equivalent resistance of R_1 (b) and R_2 (c). (d) Speculated mechanism of the HMF reduction over the Pb/PbO@C catalysts.

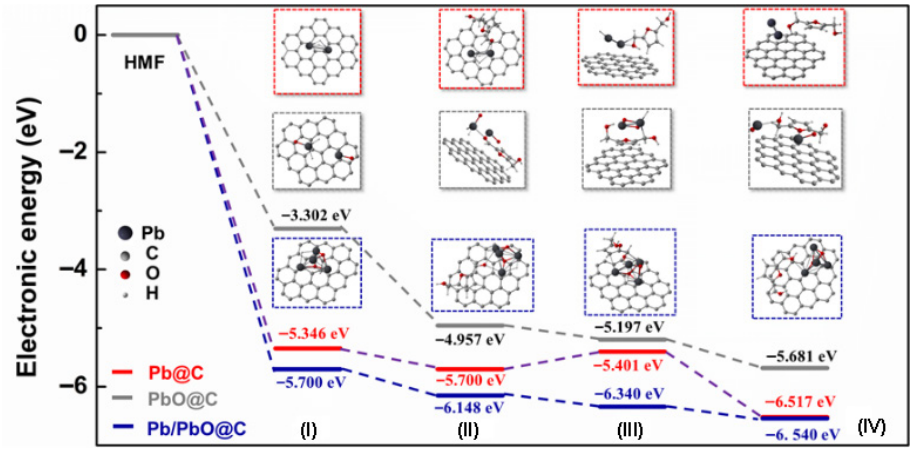

Figure 7 DFT calculations of the electrocatalytic reduction of HMF over Pb@C, Pb/PbO@C and PbO@C.

PbO@C (−5.197 eV), respectively, indicating that the synergistic effect of Pb^0 and Pb^{2+} sites in Pb/PbO@C promotes the binding of H* and HMF to form H-HMF* and thus accelerates the reaction kinetics of HMF reduction, which is consistent with our experimental results.

Based on the above analysis, it can be concluded that the superior performance of Pb/PbO@C-800 for the electrochemical reduction of HMF to BHMF stems from the rich Lewis acidic sites, strengthening the adsorption of HMF carbonyl group, thus resulting in an enhancing selectivity of BHMF. The suitable pyrolysis temperature of Pb/PbO@C-800 enhances the exposure of electron-deficient Pb^0/Pb^{2+} active sites. The appropriate electronic interaction between Pb^0/Pb^{2+} sites and support accelerates the charge transfer rate, thereby promoting the dissociation of water molecules to generate more H* species, increasing the H* coverage. The high coverage of H* species and the synergistic effect of dual-center sites substantially inhibit the recombination of H* species and promote the binding of H* and HMF to form H-HMF*, thereby accelerating the reaction kinetics of HMF reduction.

4 Conclusion

In summary, novel 2D biomass-derived Pb/PbO@C catalysts based on natural-derived humate were synthesized for the electrocatalytic reduction of HMF to BHMF using water as the hydrogen source. The optimized Pb/PbO@C-800 shows an excellent performance with high FE (91.9%) and Sel (89.7%) of BHMF. Mechanism study unveils that the excellent activity of Pb/PbO@C-800 stems from the

rich Lewis acidic sites, the maximum exposure of active site and the suitable electronic interaction of Pb^0/Pb^{2+} sites and carbon support, all of which enhance the adsorption of HMF on Pb^{2+} sites, promote the dissociation of water molecules to generate more H* species and increase the coverage of H* species on Pb^0 sites. The high coverage of H* species and the synergistic effect of dual-center sites substantially inhibit the recombination of H* species and reduce the binding energy of H* and HMF to form H-HMF*, thereby accelerating the reaction kinetics of HMF reduction. This study opens a new avenue for using abundant natural resources to prepare functional electrocatalysts and provides new clues for deeply understanding the HMF electroreduction mechanism.

Electronic Supplementary Material: Supplementary material (general information, supplementary figures and table, methods, experimental procedures, characterization data and references) is available in the online version of this article at https://doi.org/10.26599/NR.2025.94907089.

Data availability

All data needed to support the conclusions in the paper are presented in the manuscript and the Electronic Supplementary Material. Additional data related to this paper may be requested from the corresponding author upon request.

Acknowledgements

This work was supported by the National Natural Science Foundation of China (Nos. 22225501 and 52073173), the Key Research Projects of Universities in Henan Province (No. 23A530005), the National Key Laboratory of Biobased Transport Fuel Technology (No. KFKT2022002) of China, Program of Shanghai Academic/Technology Research Leader (No. 23XD1431700) and Shanghai Engineering Research Center of Specialized Polymer Materials for Aerospace (No. 18DZ2253500).

Declaration of competing interest

All the contributing authors report no conflict of interests in this work.

Author contribution statement

H. R. W.: Project administration, writing manuscript, experimental design. H. S. X.: Experimental design. Z. B. X.: Data curation, writing manuscript. project supervision. R. L. Y.: Experimental design. X. W.: Experimental design, writing manuscript. X. W. C.: Writing manuscript. L. W.: Writing manuscript. C. Y. Z.: Project design, writing manuscript, funding acquisition. W. X. Z.: Project design, writing manuscript, project supervision. Y. Y. M.: Project design and administration, writing manuscript, funding acquisition. All the authors have approved the final manuscript.

Use of AI statement

None.

References

[1] Chen, D. X.; Ding, Y. X.; Cao, X.; Wang, L. Q.; Lee, H.; Lin, G. X.; Li, W. L.; Ding, G. H.; Sun, L. C. Highly efficient biomass upgrading by a Ni-Cu electrocatalyst featuring passivation of water oxidation activity. *Angew. Chem., Int. Ed.* **2023**, *62*, e202309478.

[2] Mooraj, S.; Qi, Z.; Zhu, C.; Ren, J.; Peng, S. Y.; Liu, L.; Zhang, S. B.; Feng, S.; Kong, F. Y.; Liu, Y. F. et al. 3D printing of metal-based materials for renewable energy applications. *Nano Res.* **2021**, *14*, 2105–2132.

[3] Tian, C.; Dorakhan, R.; Wicks, J.; Chen, Z.; Choi, K. S.; Singh, N.; Schaidle, J. A.; Holewinski, A.; Vojvodic, A.; Vlachos, D. G. et al. Progress and roadmap for electro-privileged transformations of bio-derived molecules. *Nat. Catal.* **2024**, *7*, 350–360.

[4] Zhang, Y. E.; Zhu, W.; Fang, J. J.; Xu, Z. Y.; Xue, Y. R.; Liu, D.; Sui, R.; Lv, Q. Q.; Liu, X. R.; Wang, Y. S. et al. Defective Ni_3S_2 nanowires as highly active electrocatalysts for ethanol oxidative upgrading. *Nano Res.* **2022**, *15*, 2987–2993.

[5] Sendeku, M. G.; Harrath, K.; Dajan, F. T.; Wu, B. L.; Hussain, S.; Gao, N.; Zhan, X. Y.; Yang, Y.; Wang, Z. X.; Chen, C. et al. Deciphering *in-situ* surface reconstruction in two-dimensional $CdPS_3$ nanosheets for efficient biomass hydrogenation. *Nat. Commun.* **2024**, *15*, 5174.

[6] Tian, C.; Yu, J. Q.; Zhou, D. J.; Ze, H.; Liu, H. Z.; Chen, Y. J.; Xia, R.; Ou, P. F.; Ni, W. Y.; Xie, K. et al. Reduction of 5-hydroxymethylfurfural to 2,5-bis(hydroxymethyl)furan at high current density using a Ga-doped AgCu: Cationomer hybrid electrocatalyst. *Adv. Mater.* **2024**, *36*, 2312778.

[7] Zheng, Y. N.; Wang, L. Q.; Liu, H. Y.; Yang, J. Q.; Zhang, R.; Zhang, L.; Qiao, Z. A. A modular co-assembly strategy for ordered mesoporous perovskite oxides with abundant surface active sites. *Angew. Chem., Int. Ed.* **2022**, *61*, e202209038.

[8] Deng, Q.; Hou, X. M.; Zhong, Y.; Zhu, J. W.; Wang, J.; Cai, J. X.; Zeng, Z. L.; Zou, J. J.; Deng, S. G.; Yoskamtorn, T. et al. 2D MOF with compact catalytic sites for the one-pot synthesis of 2,5-dimethylfuran from saccharides via tandem catalysis. *Angew. Chem.* **2022**, *134*, e202205453.

[9] Duan, Y.; Zhang, C.; Deng, D. S.; Sui, D.; Gao, X. H.; Yang, Y. L. Hydrogenation of BHMF with controllable selectivity to tetrahydropyranone and 1-hydroxy-2,5-hexanedione under atmospheric H_2 pressure. *Green Chem.* **2023**, *25*, 1823–1834.

[10] Yuan, X.; Lee, K.; Schmidt, J. R.; Choi, K. S. Halide adsorption enhances electrochemical hydrogenolysis of 5-hydroxymethylfurfural by suppressing hydrogenation. *J. Am. Chem. Soc.* **2023**, *145*, 20473–20484.

[11] Li, Y.; Jiao, Y. Q.; Yan, H. J.; Tian, C. G.; Wu, A. P.; Fu, H. G. Recent progress in synergistic electrocatalysis for generation of valuable products based on water cycle. *Nano Res.* **2023**, *16*, 6444–6476.

[12] Chimentão, R. J.; Oliva, H.; Belmar, J.; Morales, K.; Mäki-Arvela, P.; Wärnå, J.; Murzin, D. Y.; Fierro, J. L. G.; Llorca, J.; Ruiz, D. Selective hydrodeoxygenation of biomass derived 5-hydroxymethylfurfural over silica supported iridium catalysts. *Appl. Catal. B: Environ.* **2019**, *241*, 270–283.

[13] Kumar, R.; Lee, H. H.; Chen, E.; Du, Y. P.; Lin, C. Y.; Prasanseang, W.; Solos, T.; Choojun, K.; Sooknoi, T.; Xie, R. K. et al. Facile synthesis of the atomically dispersed hydrotalcite oxide supported copper catalysts for the selective hydrogenation of 5-hydroxymethylfurfural into 2,5-bis(hydroxymethyl)furan. *Appl. Catal. B: Environ.* **2023**, *329*, 122547.

[14] Wu, Y. D.; Jiang, Y. M.; Chen, W.; Yue, X.; Dong, C. L.; Qiu, M. Y.; Nga, T. T. T.; Yang, M.; Xia, Z. C.; Xie, C. et al. Selective electroreduction of 5-hydroxymethylfurfural to dimethylfuran in neutral electrolytes via hydrogen spillover and adsorption configuration adjustment. *Adv. Mater.* **2024**, *36*, 2307799.

[15] Li, J.; Ji, K. Y.; Li, B. Y.; Xu, M.; Wang, Y.; Zhou, H.; Shi, Q. J.; Duan, H. H. Rechargeable biomass battery for electricity storage/generation and concurrent valuable chemicals production. *Angew. Chem., Int. Ed.* **2023**, *62*, e202304852.

[16] Xu, H.; Xu, G. X.; Huang, B. J.; Yan, J. B.; Wang, M.; Chen, L. S.; Shi, J. L. Zn-organic batteries for the semi-hydrogenation of biomass aldehyde derivatives and concurrently enhanced power output. *Angew. Chem., Int. Ed.* **2023**, *62*, e202218603.

[17] You, B.; Jiang, N.; Liu, X.; Sun, Y. J. Simultaneous H_2 generation and biomass upgrading in water by an efficient noble-metal-free bifunctional electrocatalyst. *Angew. Chem., Int. Ed.* **2016**, *55*, 9913–9917.
[18] Wu, W. J.; Wang, Y. F.; Du, K. M.; Liu, Q. S.; Zhou, T.; Wei, N.; Liu, G. H.; Guo, J. Enhancing the performance of catalytic membranes for simultaneous degradation of dissolved organic phosphonates and phosphorous recovery: A fit-for-purpose loose nanofiltration design. *Appl. Catal. B: Environ. Energy* **2024**, *354*, 124118.
[19] Yang, F.; Antonietti, M. Artificial humic acids: Sustainable materials against climate change. *Adv. Sci.* **2020**, *7*, 1902992.
[20] Yang, F.; Zhang, S. S.; Song, J. P.; Du, Q.; Li, G. X.; Tarakina, N. V.; Antonietti, M. Synthetic humic acids solubilize otherwise insoluble phosphates to improve soil fertility. *Angew. Chem., Int. Ed.* **2019**, *58*, 18813–18816.
[21] Klüpfel, L.; Piepenbrock, A.; Kappler, A.; Sander, M. Humic substances as fully regenerable electron acceptors in recurrently anoxic environments. *Nat. Geosci.* **2014**, *7*, 195–200.
[22] Zha, K.; Xiong, Y.; Zhang, W. Q.; Tan, M. J.; Hu, W. X.; Lin, Z.; Cheng, P.; Lu, L.; Cai, K. Y.; Mi, B. B. et al. Waste to wealth: Near-infrared/pH dual-responsive copper-humic acid hydrogel films for bacteria-infected cutaneous wound healing. *ACS Nano* **2023**, *17*, 17199–17216.
[23] Han, J.; Park, J.; Bak, S. M.; Son, S. B.; Gim, J.; Villa, C.; Hu, X. B.; Dravid, V. P.; Su, C. C.; Kim, Y. et al. New high-performance Pb-based nanocomposite anode enabled by wide-range Pb redox and zintl phase transition. *Adv. Funct. Mater.* **2021**, *31*, 2005362.
[24] Lan, T.; Wu, P.; Yin, X. Y.; Zhao, Y. F.; Liao, J. L.; Wang, D. Q.; Liu, N. Rigidity and flexibility: Unraveling the role of fulvic acid in uranyl sorption on graphene oxide using molecular dynamics simulations. *Environ. Sci. Technol.* **2023**, *57*, 10339–10347.
[25] Tana, T.; Han, P. F.; Brock, A. J.; Mao, X.; Sarina, S.; Waclawik, E. R.; Du, A. J.; Bottle, S. E.; Zhu, H. Y. Photocatalytic conversion of sugars to 5-hydroxymethylfurfural using aluminium(III) and fulvic acid. *Nat. Commun.* **2023**, *14*, 4609.
[26] Dong, Y. T.; Zhang, Z. M.; Yan, W.; Hu, X. R.; Zhan, C. H.; Xu, Y.; Huang, X. Q. Pb-modified ultrathin RuCu nanoflowers for active, stable, and CO-resistant alkaline electrocatalytic hydrogen oxidation. *Angew. Chem., Int. Ed.* **2023**, *62*, e202311722.
[27] Inaguma, Y.; Tanaka, K.; Tsuchiya, T.; Mori, D.; Katsumata, T.; Ohba, T.; Hiraki, K. I.; Takahashi, T.; Saitoh, H. Synthesis, structural transformation, thermal stability, valence state, and magnetic and electronic properties of $PbNiO_3$ with perovskite- and $LiNbO_3$-type structures. *J. Am. Chem. Soc.* **2011**, *133*, 16920–16929.
[28] Li, J.; Xie, L. S.; Pu, Z. W.; Liu, C.; Yang, M. J.; Meng, Y. Y.; Han, B.; Bu, S. X.; Wang, Y. H.; Zhang, X. L. et al. The synergistic effect of pemirolast potassium on carrier management and strain release for high-performance inverted perovskite solar cells. *Adv. Funct. Mater.* **2023**, *33*, 2301956.
[29] Du, Q.; Zhang, S. S.; Song, J. P.; Zhao, Y.; Yang, F. Activation of porous magnetized biochar by artificial humic acid for effective removal of lead ions. *J. Hazard. Mater.* **2020**, *389*, 122115.
[30] Feng, Z. Y.; Zheng, Y. H.; Wang, H. S.; Feng, C. P.; Chen, N.; Wang, S. Z. Sodium humate based double network hydrogel for Cu and Pb removal. *Chemosphere* **2023**, *313*, 137558.
[31] Ji, K. Y.; Xu, M.; Xu, S. M.; Wang, Y.; Ge, R. X.; Hu, X. Y.; Sun, X. M.; Duan, H. H. Electrocatalytic hydrogenation of 5-hydroxymethylfurfural promoted by a Ru_1Cu single-atom alloy catalyst. *Angew. Chem., Int. Ed.* **2022**, *61*, e202209849.
[32] Xiao, X. F.; Tian, X. C.; Li, J. P.; Yang, F.; Bai, R.; Zhao, F. Self-doping active sites in microbe-derived carbonaceous electrocatalysts for the oxygen reduction reaction performance. *Nano Res.* **2024**, *17*, 6803–6819.
[33] Guo, Y. L.; Li, Y. Y.; Du, X. R.; Li, L.; Jiang, Q. K.; Qiao, B. T. Pd single-atom catalysts derived from strong metal-support interaction for selective hydrogenation of acetylene. *Nano Res.* **2022**, *15*, 10037–10043.
[34] Conings, B.; Babayigit, A.; Boyen, H. G. Fire safety of lead halide perovskite photovoltaics. *ACS Energy Lett.* **2019**, *4*, 873–878.
[35] Gao, P.; Xue, Z. H.; Zhang, S. N.; Xu, D.; Zhai, G. Y.; Li, Q. Y.; Chen, J. S.; Li, X. H. Schottky barrier-induced surface electric field boosts universal reduction of NO_x^- in water to ammonia. *Angew. Chem., Int. Ed.* **2021**, *60*, 20711–20716.
[36] Tao, L.; Wang, Y. Q.; Zou, Y. Q.; Zhang, N. N.; Zhang, Y. Q.; Wu, Y. J.; Wang, Y. Y.; Chen, R.; Wang, S. Y. Charge transfer modulated activity of carbon-based electrocatalysts. *Adv. Energy Mater.* **2020**, *10*, 1901227.
[37] Yan, Q. Q.; Yin, P.; Liang, H. W. Engineering the electronic interaction between metals and carbon supports for oxygen/hydrogen electrocatalysis. *ACS Mater. Lett.* **2021**, *3*, 1197–1212.
[38] Lu, Y. X.; Dong, C. L.; Huang, Y. C.; Zou, Y. Q.; Liu, Z. J.; Liu, Y. B.; Li, Y. Y.; He, N. H.; Shi, J. Q.; Wang, S. Y. Identifying the geometric site dependence of spinel oxides for the electrooxidation of 5-hydroxymethylfurfural. *Angew. Chem., Int. Ed.* **2020**, *59*, 19215–19221.
[39] Zhang, D. F.; Chen, J. X.; Hao, Z. J.; Jiao, L.; Ge, Q. F.; Fu, W. F.; Lv, X. J. Highly efficient electrochemical hydrogenation of acetonitrile to ethylamine for primary amine synthesis and promising hydrogen storage. *Chem Catal.* **2021**, *1*, 393–406.
[40] Sanyal, U.; Yuk, S. F.; Koh, K.; Lee, M. S.; Stoerzinger, K.; Zhang, D. F.; Meyer, L. C.; Lopez-Ruiz, J. A.; Karkamkar, A.; Holladay, J. D. et al. Hydrogen bonding enhances the electrochemical hydrogenation of benzaldehyde in the aqueous phase. *Angew. Chem., Int. Ed.* **2021**, *60*, 290–296.
[41] Li, L. G.; Wang, P. T.; Shao, Q.; Huang, X. Q. Metallic nanostructures with low dimensionality for electrochemical water splitting. *Chem. Soc. Rev.* **2020**, *49*, 3072–3106.
[42] Zhang, W. F.; Qi, Y. B.; Zhao, Y.; Ge, W. X.; Dong, L.; Shen, J. H.; Jiang, H. L.; Li, C. Z. Rh-dispersed Cu nanowire catalyst for boosting electrocatalytic hydrogenation of 5-hydroxymethylfurfural. *Sci. Bull.* **2023**, *68*, 2190–2199.
[43] Cao, X.; Ding, Y. X.; Chen, D. X.; Ye, W. T.; Yang, W. X.; Sun, L. C. Cluster-level heterostructure of PMo_{12}/Cu for efficient and selective electrocatalytic hydrogenation of high-concentration 5-hydroxymethylfurfural. *J. Am. Chem. Soc.* **2024**, *146*, 25125–25136.
[44] de Luna, G. S.; Sacco, A.; Hernandez, S.; Ospitali, F.; Albonetti, S.; Fornasari, G.; Benito, P. Insights into the electrochemical reduction of 5-hydroxymethylfurfural at high current densities. *ChemSusChem* **2022**, *15*, e202102504.
[45] Xie, C.; Chen, W.; Du, S. Q.; Yan, D. F.; Zhang, Y. Q.; Chen, J.; Liu, B.; Wang, S. Y. *In-situ* phase transition of WO_3 boosting electron and hydrogen transfer for enhancing hydrogen evolution on Pt. *Nano Energy* **2020**, *71*, 104653.
[46] Yang, Y.; Xiong, Y.; Zeng, R.; Lu, X. Y.; Krumov, M.; Huang, X.; Xu, W. X.; Wang, H. S.; DiSalvo, F. J.; Brock, J. D. et al. *Operando* methods in electrocatalysis. *ACS Catal.* **2021**, *11*, 1136–1178.
[47] Wu, H. R.; Chen, X. W.; Xu, H. S.; Yang, R. L.; Wang, X.; Chen, J. Y.; Xie, Z. B.; Wu, L.; Mai, Y. Insight into the mechanism of 5-hydroxymethylfurfural electroreduction to 2,5-bis(hydroxymethyl)furan over Cu anchored N-doped carbon nanosheets. *Nano Res.* **2024**, *17*, 7991–7999.